OCCAM

OXFORD CENTRE FOR COLLABORATIVE APPLIED MATHEMATICS

Report Number 09/23

Morphological instability of a nonequilibrium icecolloid interface

by

S.S.L. Peppin, A. Majumdar and J.S. Wettlaufer

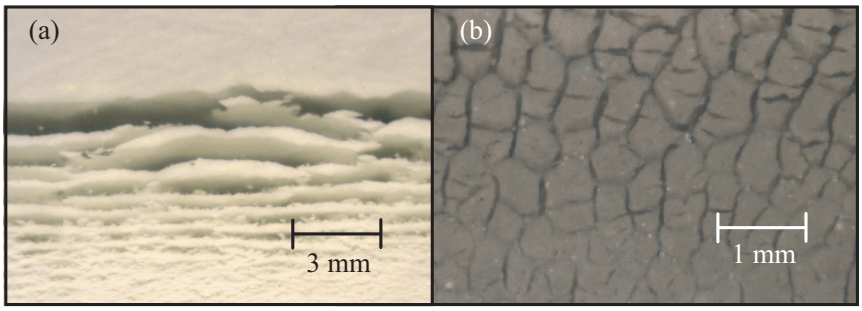

UNIVERSITY OF OXFORD

Oxford Centre for Collaborative Applied Mathematics
Mathematical Institute
24 - 29 St Giles'
Oxford
OX1 3LB
England

Morphological instability of a nonequilibrium ice–colloid interface

By S. S. L. Peppin,[1] A. Majumdar[1] and J. S. Wettlaufer[2]

[1]*OCCAM, Mathematical Institute, University of Oxford, St Giles Road, Oxford OX1 3LB, UK*

[2]*Departments of Geology & Geophysics and Physics, Program in Applied Mathematics, Yale University, New Haven, CT, 06520-8109, USA*

We assess the morphological stability of a nonequilibrium ice–colloidal suspension interface, and apply the theory to bentonite clay. An experimentally convenient scaling is employed which takes advantage of the vanishing segregation coefficient at low freezing velocities, and when anisotropic kinetic effects are included the interface is shown to be unstable to travelling waves. The potential for traveling wave modes reveals a possible mechanism for the polygonal and spiral ice lenses observed in frozen clays. A weakly nonlinear analysis yields a long-wave evolution equation for the interface shape containing a new parameter related to the highly nonlinear liquidus curve in colloidal systems. We discuss the implications of these results for the frost susceptibility of soils and the fabrication of microtailored porous materials.

Keywords: Solidification, colloidal suspensions, linear stability

1. Introduction

When a colloidal suspension such as a clay soil freezes an interesting phenomenon occurs in which the ice segregates into lenticular or dendritic shapes. For example, in soils composed mainly of silt particles the ice usually forms nearly planar layers, called *ice lenses* (Taber 1929; Watanabe and Mizoguchi 2000), whereas in a wide range of clays and colloidal suspensions, the ice can grow in several directions, producing a remarkable variety of patterns (Taber 1929; Chamberlain and Gow 1979; Brown 1984; Deville et al 2009; see Figure 1). Recently we proposed a mechanism for ice segregation in freezing colloidal suspensions based on the concept of morphological instability studied in alloys quantitatively applied to the ice–suspension interface (Peppin et al 2006; 2007; 2008). The approach relies essentially on treating a colloidal suspension as a *two-component thermodynamic system* in which the solute particles are vastly larger than the solvent, and by exploiting the physical basis for the dynamics and thermodynamics of premelting between these particles and the frozen solvent. Here, we extend this approach by incorporating the anisotropic growth kinetics of ice, and by developing a weakly nonlinear analysis of long wavelength modes to reveal evolution equations derived in the alloy setting and others.

Our previous experimental studies focused on using bentonite clay as an easily accessible and broadly relevant colloid and hence we begin in Section 2 by discussing its physicochemical properties. The freezing point depression and particle

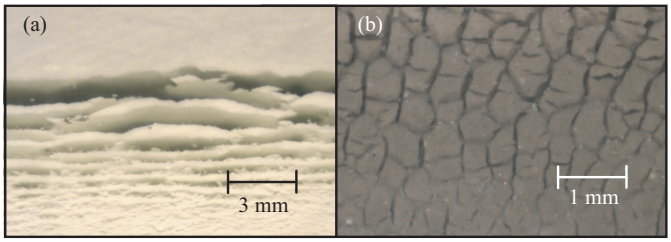

Figure 1. (a) Planar ice lenses (dark regions) formed during the solidification of water-saturated kaolinite clay (74 wt%). (b) Polygonal pattern of segregated ice (dark regions) formed during the solidification of water-saturated bentonite clay (50 wt%). The direction of freezing was from bottom to top.

diffusivity $D(\phi)$ are given as functions of particle volume fraction ϕ. It is found that over a significant range in ϕ the diffusivity is approximately constant, simplifying many aspects of the stability analysis to follow. The interfacial properties of ice are discussed in section 3, where we consider the effect of interfacial curvature on the equilibrium freezing temperature, and allow for the nonequilibrium effects of kinetic undercooling and kinetic anisotropy. Moreover, we discuss the mechanism of particle trapping and its basis for the segregation coefficient. At low freezing velocities the segregation coefficient is zero, allowing an experimentally convenient scaling to be employed in our analysis of colloidal suspensions. Due to the fact that our analysis of the thermophysical properties of bentonite suspensions allows us to construct interfacial and boundary conditions that are directly analogous to the binary alloy system, we then, in section 4, construct a model of the unidirectional solidification of such suspensions. Indeed, it is found that the clay becomes *constitutionally supercooled* under typical freezing conditions, in agreement with experimental results (Brown 1984; Peppin et al 2008). We then analyse the morphological stability of a planar steady-state ice–clay interface in section 5, and obtain an equation for the critical parameters at which the interface becomes unstable. The linear analysis predicts the possibility of travelling-wave instabilities, as found in the atomic alloy system by Young et al (1987), and we explicitly find their operative range of wavenumbers in terms of the model parameters. The structure of the linear problem suggested a long wavelength weakly nonlinear analysis yields would be fruitful. As such, we derived an evolution equation for the interface shape in this limit. In section 6 we discuss our results, describe the conditions that must be satisfied for the stable solidification of a colloidal suspension and suggest future research directions and applications to geophysical and technological systems.

2. Physicochemical properties

(*a*) *Freezing point depression*

In this section we discuss the freezing point depression of bentonite, a material for which an extensive range of experimental data is available. Figure 2 shows a system in which a macroscopic portion of ice is in equilibrium with a macroscopic quantity of unfrozen water-saturated clay. As the temperature is lowered, the ice phase grows and the particle volume fraction of the clay increases. At a critical *breakthrough* temperature T_B and volume fraction ϕ_B, ice is able to enter the pore

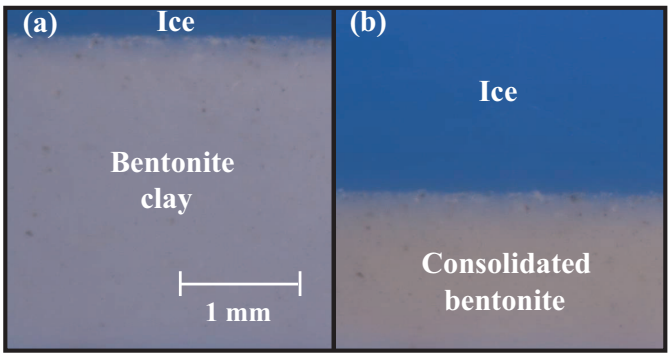

Figure 2. Quasi-static freezing of bentonite clay. In (a) the clay volume fraction is 0.02 and the temperature is near 0 °C. In (b) the temperature is reduced, and the clay has consolidated to a new higher equilibrium concentration.

space between particles (Brown and Payne 1990; Shanti et al 2006). For kaolinite clay, the ice-entry temperature is $T_B = -0.77\,^{\circ}\mathrm{C}$ (Brown and Payne 1990). As far as we are aware, the ice-entry temperature has not been measured for bentonite, though Brown and Payne (1990) found no pore ice down to at least $-8\,^{\circ}\mathrm{C}$. We note that here T_B is considered an equilibrium temperature. In this sense it is analogous to the eutectic transformation in alloys. Ice can also enter the pore space at temperatures warmer than T_B via non-equilibrium particle trapping (Wettlaufer and Worster 2006). We discuss particle trapping further in Section 3c.

Here we study relatively slow freezing velocities and temperatures above T_B, such that no pore ice is present. We also assume the ice phase is devoid of particles, in which case the freezing point depression (colloidal liquidus curve) can be obtained by equating the chemical potential of water in the unfrozen colloid (known, for example, from osmotic pressure measurements) with the chemical potential of pure ice. For temperatures near to the bulk freezing temperature T_m of pure water, and neglecting the temperature dependence of the osmotic pressure Π this leads to the relation (eg Low *et al.* 1968)

$$T_f(\phi) = T_m \left[1 - \frac{\Pi(\phi)}{\rho_w L_f}\right], \tag{2.1}$$

where ρ_w and L_f are the density and latent heat of fusion, respectively, of water. Experimental measurements of the osmotic pressure of bentonite can be fit well to an equation of the form:

$$\Pi(\phi) = \frac{\phi}{v_p} k_B T_m Z(\phi)\ , \tag{2.2}$$

where $v_p = \frac{4}{3}\pi R^3$ is the volume of a particle of radius R (Here $0.5\,\mu$m), k_B is Boltzmann's constant and

$$Z(\phi) = \frac{1 + a_1\phi + a_2\phi^2 + a_3\phi^3 + a_4\phi^4}{1 - \phi/\phi_p}, \tag{2.3}$$

is the compressibility factor, where $a_1 = 1 \times 10^7,\ a_2 = 2 \times 10^9,\ a_3 = 3 \times 10^9, a_4 = -8 \times 10^9$ and $\phi_p = 0.64$ are fitting parameters (Peppin et al 2008).

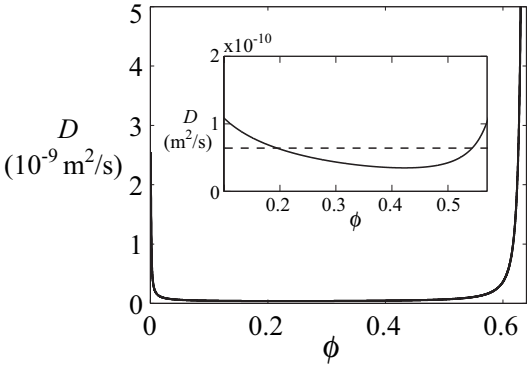

Figure 3. Calculation of the diffusivity of bentonite using the generalized Stokes-Einstein relation (2.4). The inset shows the diffusivity at intermediate concentrations along with the constant approximation $D = 6.4 \times 10^{-11}\,\mathrm{m^2\,s^{-1}}$ (dashed line) used in Section 4b.

(*b*) *Permeability and diffusivity*

To obtain the particle diffusivity we use a generalized form of the Stokes-Einstein relation

$$D = \phi \frac{k}{\eta} \left(\frac{\partial \Pi}{\partial \phi} \right)_{T,P}, \tag{2.4}$$

where D is the particle diffusivity, k is the permeability, η is the fluid viscosity, T is the absolute temperature and P is the mixture pressure (Russel et al 1989; Peppin et al 2006). Given measurements of the permeability and osmotic pressure Π, equation (2.4) can be used to determine the diffusivity as a function of volume fraction. Experimental measurements of the permeability of bentonite can be fit to the equation (Peppin et al 2008)

$$k(\phi) = \frac{2R^2}{9\phi} \left(1 + 3.1 \times 10^8 \phi^{2.6}\right)^{-1}. \tag{2.5}$$

Hence, with (2.2), (2.3) and (2.5), and using a value of $\eta = 0.002\,\mathrm{kg\,m^{-1}\,s^{-1}}$ for the viscosity of water at 0 °C (Hallett 1963), equation (2.4) yields the diffusivity of bentonite as a function of ϕ, plotted in figure 3. Interestingly, the diffusivity remains approximately constant over a large range in volume fraction before finally diverging near the random close packing limit ϕ_p. This property of the diffusivity will enable us to simplify the stability analysis in section 5.

3. Surface properties of ice

(*a*) *Interfacial curvature*

In this section we discuss the effect of curvature on the ice–colloid interface temperature, in the case where the macroscopic radius of curvature of the interface is much larger than the hydrodynamic radius of a particle. The thermodynamic conditions for equilibrium are then given by (eg Defay and Prigogine 1966):

$$T_i = T_c = T_{Ie}, \tag{3.1}$$

$$P_c - P_i = \gamma K, \tag{3.2}$$

$$\mu_1^i = \mu_1^c, \tag{3.3}$$

where T_i is the temperature of the ice; T_c is the temperature of the colloid; T_{Ie} is the equilibrium interface temperature; μ_1^i is the chemical potential of the ice; μ_1^c is the chemical potential of water in the colloid; P_i is the pressure of the ice; P_c is the pressure of the colloid; γ is the ice-colloid surface energy; and K is twice the mean interfacial curvature (defined to be negative for a convex finger of ice extending into the colloid phase). Not much is known about the concentration dependence of γ, though limited experimental evidence indicates that the dependence is weak, or at least bounded as the concentration increases (Schramm and Helper 1994; Dong and Johnson 2004). In the following we take γ to be a constant.

We assume that the densities and specific entropies (entropy per unit mass) of ice and water and that the osmotic pressure $\Pi(\phi)$ of the clay are independent of temperature and pressure over the range of our study, and that there are no anisotropic stresses on the ice. Whence, the chemical potentials can be expanded about the planar ice-water freezing temperature T_m and atmospheric pressure P_{atm} to yield (eg Prigogine and Defay 1954, Acker et al 2001)

$$\mu_1^i(T_{Ie}, P_i) = \mu_1^0(T_m, P_{atm}) + \nu_i(P_i - P_{atm}) - s_i(T_{Ie} - T_m), \tag{3.4}$$

$$\mu_1^c(T_{Ie}, P_c, \phi) = \mu_1^0(T_m, P_{atm}) + \nu_w(P_c - P_{atm}) - s_w(T_{Ie} - T_m) - \nu_w\Pi(\phi), \tag{3.5}$$

where $\nu_i = 1/\rho_i$, $\nu_w = 1/\rho_w$ are the specific volumes of ice and water, respectively; s_i, s_w are the specific entropies of ice and water; and μ_1^0 is the chemical potential of pure ice/water at T_m and P_{atm}. Inserting (3.4), (3.5) and (3.2) into (3.3) yields

$$T_{Ie} = T_m\left(1 - \frac{\Pi}{\rho_w L_f} + \frac{\gamma K}{\rho_i L_f}\right). \tag{3.6}$$

In obtaining (3.6) we used $T_m(s_w - s_i) = L_f$ and we have ignored a term, $(P_c - P_{atm})(\nu_i - \nu_w)/L_f$, which represents the effect of pressure melting on the interfacial temperature and can usually be neglected relative to the other terms (See eqn 2 of Dash et al 2006). For a planar interface equation (3.6) reduces to (2.1).

(*b*) *Premelting, kinetic undercooling and kinetic anisotropy*

When the interface between ice and a foreign particle is studied on the nanometre scale, it is found that the ice is not in direct contact with the particle, but rather a thin film of premelted water exists between the two surfaces (Dash et al 2006). During solidification, fluid flows around the particle and into the film enabling the ice to grow. Viscous dissipation in the film leads to a kinetic undercooling (Wettlaufer and Worster 2006), which can be represented on the macroscopic scale by

$$V_n = V_n(\Delta T), \tag{3.7}$$

where V_n is the ice velocity in a direction normal to the freezing interface and $\Delta T = T_{Ie} - T_I$ is the undercooling. The nonequilibrium interface temperature is T_I, and T_{Ie} is the equilibrium ($V_n = 0$) temperature given by (3.6). If the surface properties are anisotropic, as is the case for ice (eg Nagashima and Furukawa 1997),

then some orientations of the interface will grow faster than others, and we must write

$$V_n = V_n(\Delta T, h_x), \tag{3.8}$$

where $h(x)$ is the height of the curved interface above the planar location and the subscript x denotes differentiation with respect to x. In the simplest case (small V_n) equation (3.8) can be written in linear form as

$$V_n = \kappa_u \Delta T + \kappa_a h_x, \tag{3.9}$$

where κ_u and κ_a are material-dependent constants accounting for kinetic undercooling and kinetic anisotropy. Solving (3.9) for T_I gives, with (3.6) and (2.1),

$$T_I = T_f(\phi_I) + \frac{T_m \gamma}{\rho_i L_f} K - \kappa_u^{-1} V_n + \frac{\kappa_a}{\kappa_u} h_x, \tag{3.10}$$

where ϕ_I is the particle volume fraction at h. Equation (3.10) gives the ice–colloid interface temperature when the the system is not at equilibrium and the interface is curved and moving. In terms of $h(x)$ the interfacial curvature can be written as

$$K = \frac{h_{xx}}{(1 + h_x^2)^{3/2}}. \tag{3.11}$$

There is little experimental data on κ_u or κ_a for colloidal particles. For $1.1\,\mu$m silica microspheres Watanabe (2002) has obtained $\kappa_u = 0.43\,\mu\mathrm{m\,s^{-1}\,{}^\circ C^{-1}}$. For bentonite and kaolinite no measurements of κ_u or κ_a are available. Therefore in the following we use $\kappa_u = 0.43\,\mu\mathrm{m\,s^{-1}\,{}^\circ C^{-1}}$ and study the effect of a range of κ_a values.

(c) *Particle trapping and the segregation coefficient*

The segregation coefficient k_s is defined as the ratio of particle concentration in the ice phase to the particle concentration in the clay phase at the ice–clay interface. In obtaining equations (2.1) and (3.6) it has been assumed that $k_s = 0$ (*i.e.* the ice is assumed pure). This is an excellent approximation when $V \to 0$ and $T > T_B$. When $V \neq 0$ many theoretical and experimental studies have shown that, above a critical freezing velocity V_c, the particles are engulfed by the ice (Uhlmann et al 1964; Cisse and Bolling 1971; Rempel and Worster 1999). This suggests that $k_s \to 1$ for $V \gg V_c$. Experimental data indicates that for submicron hydrophilic particles, $V_c \gg 10\,\mu\mathrm{m\,s^{-1}}$ (Cisse and Bolling 1971). In the present work we consider freezing velocities much less than V_c, so that the particles are completely rejected by the ice and $k_s = 0$.

4. Unidirectional solidification

(a) *Formulation*

Figure 4 illustrates the system to be studied. A layer of colloid of initial volume fraction ϕ_0 is placed to thickness L_0 in a glass cell between two fixed temperature blocks that produce a temperature gradient G_T, with $T_H > T_C$, where T_C is below the liquidus temperature $T_f(\phi_0)$ of the bulk suspension. The cell is moved through the blocks at a fixed speed V ($\ll V_c$). All of the particles will therefore be

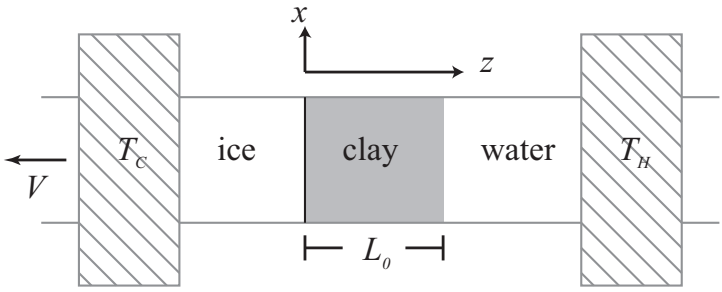

Figure 4. Schematic of a unidirectional solidification stage. A clay suspension of thickness L_0 is placed above an ice interface contained in a glass cell. The cell is moved in the $-z$ direction at speed V through two cooling blocks at temperatures T_C and T_H.

pushed ahead by the growing ice, and if the interface remains stable a steady-state will eventually develop. In the following we determine a relationship amongst the parameters V, ϕ_0, L_0 and G_T that separates the stable and unstable states.

We assume that the sample is contained within thick transparent plates with high thermal conductivity, such that heat flow is mainly through the plates and latent heat effects can be neglected; the so-called frozen temperature approximation (Caroli et al 1982; Davis 2001). In such a case the cooling blocks induce a constant linear temperature profile:

$$T(z) = T_i + G_T z, \tag{4.1}$$

where T_i is the temperature of the stable planar interface. From (3.10) T_i can be written as

$$T_i = T_f(\phi_i) - \kappa_u^{-1} V, \tag{4.2}$$

where ϕ_i is the particle concentration at the planar ($z = 0$) interface. The first term in (4.2) accounts for the equilibrium freezing point depression while the second term is the nonequilibrium kinetic undercooling.

For simplicity we neglect density differences between ice, water and particles, and take $\rho_i = \rho_w = \rho$. In a frame of reference moving at the pulling speed V, the equation describing conservation of colloid mass is

$$\phi_t - V\phi_z = \nabla \cdot D(\phi)\nabla\phi, \tag{4.3}$$

where the subscripts t and z denote differentiation with respect to time and the coordinate parallel to the growth direction. Conservation of mass at the interface $z = h(x, t)$ is given by

$$\phi_I V_n = -D(\phi)\nabla\phi \cdot \mathbf{n} \qquad (z = h), \tag{4.4}$$

where ϕ_I is the particle concentration at $z = h$,

$$V_n = \frac{V + h_t}{\sqrt{1 + h_x^2}} \tag{4.5}$$

is the speed of the deforming interface in the normal direction, and

$$\mathbf{n} = \frac{(-h_x, 1)}{\sqrt{1 + h_x^2}} \tag{4.6}$$

is the unit normal to the interface. The far-field boundary condition on (4.3) is

$$\phi \to 0, \qquad (z \to \infty). \tag{4.7}$$

The temperature at the perturbed interface is given by equation (3.10).

(*b*) *Steady state*

There exists a steady-state solution of the governing equations with a planar interface $h = 0$. The temperature field is given by equations (4.1) and (4.2). The steady-state concentration profile can be obtained by integrating (4.3) from 0 to z using (4.4) as a boundary condition to yield

$$\frac{\mathrm{d}\phi}{\mathrm{d}z} = -\frac{V\phi}{D(\phi)}. \tag{4.8}$$

A boundary condition for (4.8) at $z = 0$ can be obtained by using global mass conservation in the form

$$\int_0^\infty \phi \mathrm{d}z = \phi_0 L_0 = -\frac{1}{V}\int_{\phi_i}^0 D(\phi)\mathrm{d}\phi, \tag{4.9}$$

where ϕ_i is the volume fraction at the planar interface. As noted in section 2b, over a large range in ϕ the diffusivity is approximately constant, in which case equation (4.9) can be solved to give $\phi_i = \phi_0 L_0 V/D$, and (4.8) then yields

$$\phi = \phi_i \mathrm{e}^{-\frac{V}{D}z}. \tag{4.10}$$

Figure 5 shows predicted profiles of volume fraction, temperature and freezing temperature for a bentonite clay having initial volume fraction $\phi_0 = 0.1$, freezing velocity $V = 0.05\,\mu\mathrm{m\,s^{-1}}$ in a temperature gradient $G_T = 1\,^\circ\mathrm{C\,mm^{-1}}$ and three different initial layer thicknesses. The upper and lower solid lines in each figure show the concentration and temperature profiles, respectively, while the dash-dotted line is the freezing temperature $T_f(\phi)$. As the initial layer thickness increases the steep concentration gradient leads to a situation where, for a certain distance ahead of the freezing interface, the temperature is below the freezing temperature, and the suspension is thermodynamically (constitutionally) supercooled. The concentration profile predicted by using the constant diffusivity $D = 6.4\times10^{-11}\,\mathrm{m^2\,s^{-1}}$ from figure 3 is shown by the dotted curves in figure 5. When the volume fraction everywhere in the system is lower than 0.5 the comparison is very good. In the stability analysis to follow we treat cases where ϕ is less than 0.5, so that D can be approximated as a constant.

5. Stability Analysis

(*a*) *Linear Stability*

Now we carry out a linear stability analysis of our governing system of equations (4.3)–(4.7) which admit the steady-state solution (4.10) with a planar interface $h = 0$. We scale all lengths in the system with $\delta_\phi = L_0\phi_0$, velocities with V,

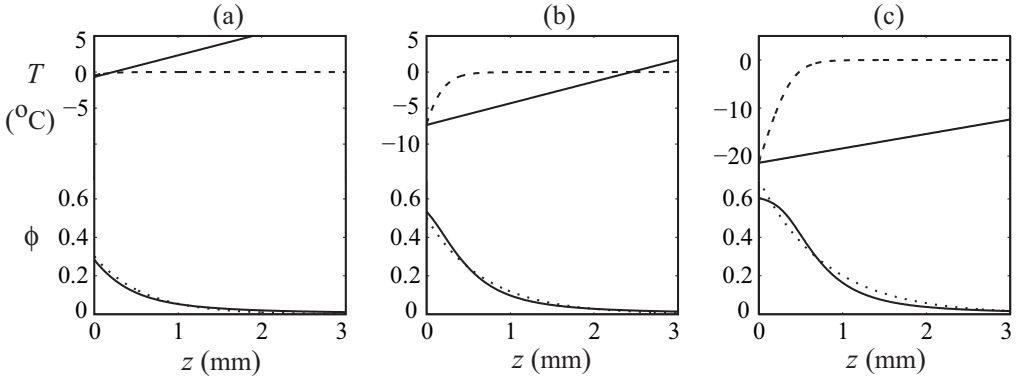

Figure 5. Steady-state temperature and concentration profiles during unidirectional solidification of bentonite clay having initial volume fraction $\phi_0 = 0.1$, freezing velocity $V = 0.05\,\mu\mathrm{m\,s^{-1}}$, temperature gradient $G_T = 1\,^\circ\mathrm{C\,mm^{-1}}$ and three layer thicknesses L_0. In (a) $L_0 = 5\,\mathrm{mm}$, (b) $L_0 = 8.5\,\mathrm{mm}$ and (c) $L_0 = 12\,\mathrm{mm}$. The upper portion of each figure shows the temperature (solid) and colloidal liquidus temperature (dashed) as functions of position away from the ice interface. The lower portion of each figure shows the corresponding concentration profile (solid). The dotted lines show the concentration profiles obtained by using a constant value for the diffusivity.

time with $\delta_t = L_0\phi_0/V$ and concentrations with $\delta_\phi G_\phi = -\delta_\phi \phi_i V/D$ where $G_\phi = \frac{d\bar{\phi}}{dz}|_{z=0} = -\phi_i V/D$. We define dimensionless variables, denoted by the superscript $*$, as follows,

$$x^* = \frac{x}{\delta_\phi},\ z^* = \frac{z}{\delta_\phi},\ h^* = \frac{h}{\delta_\phi},\ t^* = \frac{t}{\delta_t},\ \phi^* = \frac{\phi}{\delta_\phi G_\phi}. \tag{5.1}$$

There are five associated non-dimensional groups in the system; the Peclet number

$$Pe = \frac{\phi_0 L_0 V}{D}; \tag{5.2}$$

the morphological number

$$M = \frac{T_{f\phi} G_\phi}{G_T}, \tag{5.3}$$

where $T_{f\phi} = \frac{dT_f}{d\phi}|_{\phi=\phi_i}$ and G_T is the imposed thermal gradient; Γ, which measures the effects of surface energy

$$\Gamma = \frac{T_m \gamma}{\delta_\phi^2 G_\phi T_{f\phi} \rho L_f}; \tag{5.4}$$

a kinetic undercooling parameter $\hat{\kappa}_u$ given by

$$\hat{\kappa}_u = \frac{1}{\kappa_u \delta_t G_\phi T_{f\phi}}; \tag{5.5}$$

and the kinetic anisotropy parameter $\hat{\kappa}_a$ defined by

$$\hat{\kappa}_a = \frac{\kappa_a}{\kappa_u \delta_\phi G_\phi T_{f\phi}}. \tag{5.6}$$

When we substitute (5.1) into the system (4.3)–(4.7), the dimensionless governing equation becomes

$$\phi_t - \phi_z = \frac{1}{Pe}\left(\phi_{xx} + \phi_{zz}\right), \tag{5.7}$$

where for convenience we have dropped the stars from the re-scaled variables. The equation is subject to the dimensionless boundary conditions

$$\phi\left(1 + h_t\right) = -\frac{1}{Pe}\left(\phi_z - \phi_x h_x\right) \qquad (z = h) \tag{5.8}$$

$$\phi \to 0 \text{ as } z \to \infty, \tag{5.9}$$

where the nonlinear terms in h_x have been neglected.

We define the dimensionless quantity

$$\Delta T_f(\phi_I) = \frac{T_f(\phi_I) - T_f(\phi_i)}{\delta_\phi G_\phi T_{f\phi}} \tag{5.10}$$

which is proportional to the difference in the freezing point depression at the perturbed interface $z = h$, and that at the unperturbed interface $z = 0$. If we recall from (4.1) that the non-equilibrium temperature of the perturbed interface, T_I, is related to $T_f(\phi_i)$ by

$$T_I = T_f(\phi_i) - \frac{V}{\kappa_u} + G_T \delta_\phi h \ , \tag{5.11}$$

then it is seen that after substituting (5.10) and (5.11) into (3.10), we obtain the following equation that must be satisfied at the perturbed interface:

$$\Delta T_f(\phi_I) - \frac{1}{M}h + \Gamma h_{xx} - \hat{\kappa}_u h_t + \hat{\kappa}_a h_x = 0 \qquad (z = h). \tag{5.12}$$

The scaled basic state of the system (5.7)–(5.9) is given by

$$\begin{aligned} h_0 &= 0 \\ \phi_0 &= -\frac{1}{Pe}\mathrm{e}^{-Pez}. \end{aligned} \tag{5.13}$$

In the usual manner we impose small perturbations of the basic state as

$$\phi = \phi_0 + \phi^{'} \tag{5.14}$$

$$h = h_0 + h^{'}. \tag{5.15}$$

Inserting (5.14) and (5.15) into the governing equations, linearizing in the perturbed quantities, Taylor expanding the boundary conditions about $z = 0$, and seeking normal mode solutions of the form

$$\left(\phi^{'}, h^{'}\right) = \left(\phi_1(z), h_1\right)\mathrm{e}^{\sigma t + \mathrm{i}\alpha x} \tag{5.16}$$

where α is real and $\sigma = \sigma_R + \mathrm{i}\sigma_I$, leads to the following characteristic equation for the growth rate σ

$$\sigma = \frac{1}{2}\left\{Pe - \alpha^*\right\}\left\{\frac{1}{M} - 1 + \Gamma\alpha^2 + \sigma\hat{\kappa}_u - \mathrm{i}\alpha\hat{\kappa}_a\right\}, \tag{5.17}$$

where $\alpha^* = \sqrt{Pe^2 + 4Pe\sigma + 4\alpha^2}$. Since α^* is a complex number, we can explicitly compute the corresponding real and imaginary parts leading to the following coupled system of equations for the growth rate σ:

$$\begin{aligned}\sigma_R &= \frac{1}{2}\left\{Pe - \mathrm{Re}(\alpha^*)\right\}\left\{\frac{1}{M} - 1 + \Gamma\alpha^2 + \sigma_R\hat{\kappa}_u\right\} + \frac{1}{2}\mathrm{Im}(\alpha^*)(\sigma_I\hat{\kappa}_u - \alpha\hat{\kappa}_a)\\ \sigma_I &= \frac{1}{2}\left\{Pe - \mathrm{Re}(\alpha^*)\right\}(\sigma_I\hat{\kappa}_u - \alpha\hat{\kappa}_a) - \frac{1}{2}\mathrm{Im}(\alpha^*)\left\{\frac{1}{M} - 1 + \Gamma\alpha^2 + \sigma_R\hat{\kappa}_u\right\},\end{aligned} \tag{5.18}$$

where

$$\begin{aligned}\mathrm{Re}(\alpha^*) &= \frac{1}{\sqrt{2}}\left[\sqrt{(Pe^2 + 4Pe\sigma_R + 4\alpha^2)^2 + 16Pe^2\sigma_I^2} + Pe^2 + 4\alpha^2 + 4Pe\sigma_R\right]^{\frac{1}{2}}\\ \mathrm{Im}(\alpha^*) &= \frac{1}{\sqrt{2}}\left[\sqrt{(Pe^2 + 4Pe\sigma_R + 4\alpha^2)^2 + 16Pe^2\sigma_I^2} - (Pe^2 + 4\alpha^2 + 4Pe\sigma_R)\right]^{\frac{1}{2}}.\end{aligned} \tag{5.19}$$

Assuming exchange of stabilities, the marginal stability curves are given by $\sigma_R = 0$. From (5.19) this gives

$$\left\{Pe - \mathrm{Re}(\alpha^*)\right\}\left\{\frac{1}{M} - 1 + \Gamma\alpha^2\right\} + \mathrm{Im}(\alpha^*)(\sigma_I\hat{\kappa}_u - \alpha\hat{\kappa}_a) = 0. \tag{5.20}$$

One can analyze (5.20) explicitly in one simple case given by

$$\sigma_I = \hat{\kappa}_a = 0.$$

Then $Pe - \mathrm{Re}(\alpha^*) < 0$ so that the condition $\sigma_R = 0$ is equivalent to

$$M = \frac{1}{1 - \alpha^2\Gamma} \tag{5.21}$$

and (5.21) is the equation of the marginal stability curve for $\sigma_I = \hat{\kappa}_a = 0$.

Consider the relation

$$\sigma_R = \frac{1}{2}\left(Pe - \sqrt{Pe^2 + 4Pe\sigma_R + 4\alpha^2}\right)\left\{\frac{1}{M} - 1 + \Gamma\alpha^2 + \sigma_R\hat{\kappa}_u\right\}$$

from (5.18). In principle, this yields a smooth function $\sigma_R\left(Pe, M, \Gamma, \alpha, \hat{\kappa}_u\right)$ such that $\sigma_R = 0$ on the marginal stability curve (5.21). If we move slightly above the curve, say $M = \frac{1}{1-\alpha^2\Gamma} + \epsilon$, where $\epsilon << 1$ is small, then we have $|\sigma_R| << 1$ and

$$\sigma_R = \frac{1}{2}\frac{\left(Pe - \sqrt{Pe^2 + 4Pe\sigma_R + 4\alpha^2}\right)\left(\frac{1}{M} - 1 + \Gamma\alpha^2\right)}{\left(1 - \hat{\kappa}_u\frac{1}{2}\left(Pe - \sqrt{Pe^2 + 4Pe\sigma_R + 4\alpha^2}\right)\right)}, \tag{5.22}$$

again from (5.18). For a fixed $\alpha > 0$, because $|\sigma_R|$ is much smaller than the either Pe, α for $M = \frac{1}{1-\alpha^2\Gamma} + \epsilon$, we have $Pe - \sqrt{Pe^2 + 4Pe\sigma_R + 4\alpha^2} < 0$. This immediately shows that the right-hand side of (5.22) is positive and therefore $\sigma_R > 0$. A similar

analysis shows that when we move below the marginal stability curve, say when $M = \frac{1}{1-\alpha^2\Gamma} - \epsilon$, then the right-hand side of (5.22) is necessarily negative and consequently $\sigma_R < 0$. Since for fixed $\{Pe, \Gamma, \hat{\kappa}_u\}$, σ_R in (5.22) is a smooth function of M and α and $\sigma_R = 0$ on the marginal stability curve (5.21), we deduce that σ_R has fixed sign on either side of the marginal stability curve and

$$M > \frac{1}{1-\alpha^2\Gamma} \Leftrightarrow \sigma_R > 0 \text{ and}$$
$$M < \frac{1}{1-\alpha^2\Gamma} \Leftrightarrow \sigma_R < 0. \tag{5.23}$$

The region above the curve corresponds to the region of instability whereas we have the region of stability below the curve. We can use this analysis near the point $(\alpha, M) = (0, 1)$. It follows straightaway from (5.23) that constitutional supercooling $(M > 1)$ leads to instability. That is, $\sigma_R > 0$ for $M > 1$ and $\sigma_R < 0$ for $M < 1$. Further, one can use (5.21) to study the effect of surface energy on the stability of the planar interface through the parameter Γ. We note that from (5.21) M diverges as $\alpha^2 \to \frac{1}{\Gamma}^-$. As Γ increases, the marginal stability curves translate vertically upwards in the (α, M)-plane and the region of stability beneath the marginal stability curve grows in size i.e. the planar interface is stable for a larger range of parameter values (α, M).

The parameter $\hat{\kappa}_a$ has a stabilizing effect as can be seen from (5.20). One can re-write (5.20) as

$$\left\{\frac{1}{M} - 1 + \Gamma\alpha^2\right\} + \frac{\mathrm{Im}\left(\sqrt{Pe^2 + \mathrm{i}4Pe\sigma_I + 4\alpha^2}\right)}{Pe - \mathrm{Re}\left(\sqrt{Pe^2 + \mathrm{i}4Pe\sigma_I + 4\alpha^2}\right)}(\sigma_I\hat{\kappa}_u - \alpha\hat{\kappa}_a) = 0$$

and since $\mathrm{Im}\left(\sqrt{Pe^2 + \mathrm{i}4Pe\sigma_I + 4\alpha^2}\right) > 0$ and $Pe - \mathrm{Re}\left(\sqrt{Pe^2 + \mathrm{i}4Pe\sigma_I + 4\alpha^2}\right) < 0$ for fixed $\alpha \neq 0$, one can see that $\hat{\kappa}_a > 0$ translates the marginal stability curves vertically upwards compared to the curve (5.21) with $\hat{\kappa}_a = 0$. Therefore, the range of stability grows in size as $\hat{\kappa}_a$ is increased.

The marginal stability curves for bentonite with $\hat{\kappa}_a \neq 0$ are computed numerically and shown in Figure 6. The parameter values shown there lead to the dimensionless groups $Pe = 0.5$, $\Gamma = 1 \times 10^{-5}$ and $\hat{\kappa}_u = 0.02$, with $\hat{\kappa}_a$ ranging from 0 to 0.5. Instability is predicted to occur when $M > 1$, in agreement with experimental data (figure 7). Interestingly, as $\hat{\kappa}_a$ increases above about 0.45, a second short-wavelength mode develops. For this mode, which could be analyzed in terms of cubic normal forms (Wettlaufer 1992), $\sigma_I \neq 0$ and hence the perturbations travel along the interface. This result could potentially explain the intriguing *spiral* and *polygonal* ice lenses observed in freezing bentonite (Taber 1929; Peppin et al 2007). Indeed, the combination of the onset of unstable modes translating parallel to the interface with the local space-time variation in the compression of the colloidal suspension could conspire to create such patterns. Experimental measurements of $\hat{\kappa}_a$ for clays and colloidal suspensions may enable quantitative comparisons to be made of critical freezing velocities for the onset of such travelling waves.

(*b*) *Evolution equation for the interface*

The structure of the linear stability diagrams suggest that the nonlinear stability of a long-wavelength mode should be assessed and hence we examine (5.7)–(5.9)

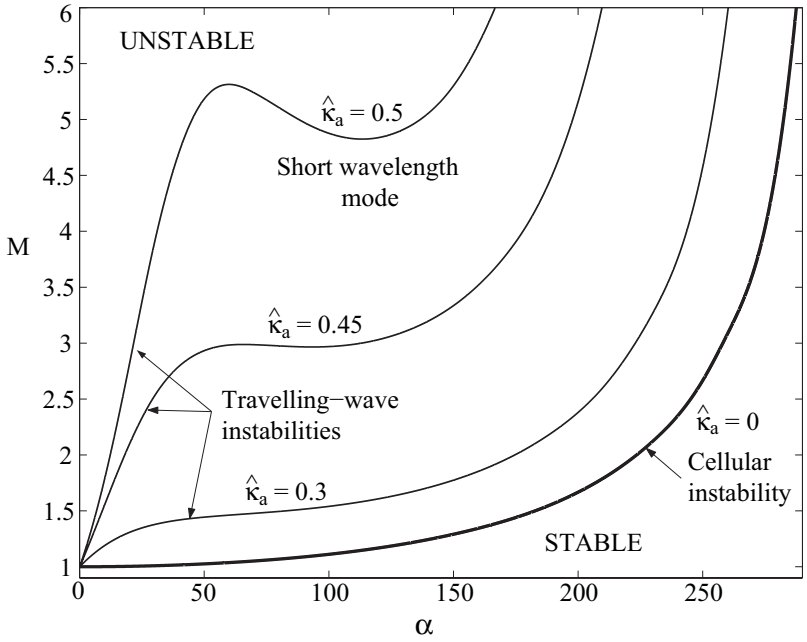

Figure 6. Bentonite stability diagram. These curves are generated using the parameter values $\phi_0 = 0.1$, $L_0 = 3.6\,\mathrm{mm}$, $V = 0.1\,\mu\mathrm{m\,s^{-1}}$, $D = 6.4 \times 10^{-7}\,\mathrm{cm^2\,s^{-1}}$, $\kappa_u = 0.34\,\mu\mathrm{m\,s^{-1}\,{}^\circ C^{-1}}$, and κ_a ranging from 0 to $2.7\,\mu\mathrm{m\,s^{-1}}$, and hence $Pe = 0.5$, $\Gamma = 1 \times 10^{-5}$, $\hat{\kappa}_u = 0.02$ and for several values of the kinetic anisotropy parameter $\hat{\kappa}_a$. Above the curves the ice–colloidal suspension is unstable while below the curves it is stable. For nonzero values of $\hat{\kappa}_a$ the interface is unstable to travelling waves.

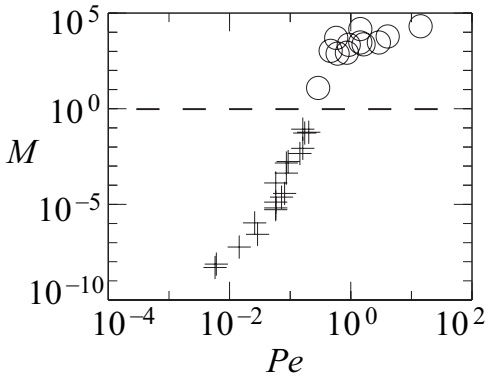

Figure 7. Bentonite regime diagram. Crosses and circles represent directional solidification experiments where the ice–clay interface was stable and unstable, respectively (Peppin et al 2008).

near the instability threshold of $M = 1$ and $\alpha = 0$ by setting

$$\alpha \approx 0;\ M = 1 + s\epsilon \tag{5.24}$$

where ϵ is a small positive number and s is a sign parameter i.e. $s = -1$(subcritical) and $s = +1$ (supercritical). We re-scale the governing equations (5.7)–(5.9) and (5.12) by introducing the variables (Sivashinsky 1983; Young et al 1987)

$$X = \sqrt{\epsilon}x^*,\ Z = z^*,\ H = \frac{1}{\epsilon}h^*,\ \Phi = \phi^*,\ T = \epsilon^2 t^*,\ \bar{\kappa}_u = \frac{1}{\sqrt{\epsilon}}\hat{\kappa}_u,\ \bar{\kappa}_a = \frac{1}{\sqrt{\epsilon}}\hat{\kappa}_a, \tag{5.25}$$

where the dimensionless variables are defined in (5.1). In terms of the re-scaled variables (5.25), the governing system for Φ becomes

$$\begin{aligned}
&\epsilon^2\Phi_T - \Phi_Z = \frac{1}{Pe}\left(\epsilon\Phi_{XX} + \Phi_{ZZ}\right)\\
&\Phi\left(1+\epsilon^3 H_T\right) = -\frac{1}{Pe}\left(\Phi_Z - \epsilon^2\Phi_X H_X\right) \quad Z = \epsilon H\\
&\Delta T_f - \frac{\epsilon}{1+s\epsilon}H + \epsilon^2\Gamma H_{XX} - \epsilon^{7/2}\bar{\kappa}_u H_T + \epsilon^2\bar{\kappa}_a H_X = 0 \quad Z = \epsilon H\\
&\Phi \to 0 \quad Z \to \infty.
\end{aligned} \tag{5.26}$$

We seek solutions as a power series in ϵ as

$$\begin{aligned}
\Phi &= \Phi_0 + \epsilon\Phi_1 + \epsilon^2\Phi_2 + \epsilon^3\Phi_3 + \ldots,\\
H &= H_0 + \epsilon H_1 + \epsilon^2 H_2 + \ldots,
\end{aligned} \tag{5.27}$$

where $\Phi_0 = -\frac{1}{Pe}\mathrm{e}^{-PeZ}$ and $H = 0$ is the planar interface solution. Inserting (5.27) into (5.26) and solving the system up to $O(\epsilon^3)$, we obtain the following explicit expressions for Φ_1 and Φ_2

$$\begin{aligned}
&\Phi_1 = 0,\\
&\Phi_2 = \left(\frac{H_0^2}{2}\left(Pe+\omega\right) - sH_0 - \Gamma H_{0XX} - \bar{\mu}_L H_{0X}\right)\mathrm{e}^{-PeZ},
\end{aligned} \tag{5.28}$$

and the following evolution equation for the interface shape $H_0 \equiv \mathcal{H}$ at order ϵ:

$$Pe\mathcal{H}_T + s\mathcal{H}_{XX} + \Gamma\mathcal{H}_{XXXX} + \bar{\kappa}_a\mathcal{H}_{XXX} - \left(Pe+\omega\right)\left(\mathcal{H}\mathcal{H}_X\right)_X = 0, \tag{5.29}$$

where $\omega = Pe^2 T_{f\phi\phi}/T_{f\phi}$ is a measure of the nonlinearity of the freezing temperature curve. The manipulations are similar to those in Young et al (1987) and we omit the details here for brevity.

Equation (5.29) has the operator structure of the long wavelength equation derived by Young et al (1987) but with additional parameters related to the physics of colloidal suspensions. In particular the finite consolidation layer leads to a Peclet number that does not appear in their semi-infinite system, and the parameter ω is a consequence of the highly nonlinear liquidus curve.

We can study the linear stability of the planar interface by taking the ansatz $\mathcal{H} = \delta\mathrm{e}^{\sigma T + \mathrm{i}aX}$ where a is real, $\sigma = \sigma_R + \mathrm{i}\sigma_I$ is the growth rate, $\delta \ll 1$ is a positive constant, and we neglect nonlinear terms of order δ^2. We substitute this ansatz into (5.29) and obtain

$$\sigma_R + \mathrm{i}\sigma_I + a^4\frac{\Gamma}{Pe} - \mathrm{i}a^3\frac{\bar{\kappa}_a}{Pe} - \frac{s}{Pe}a^2 = 0. \tag{5.30}$$

Equating imaginary terms gives

$$\sigma_I = a^3 \frac{\bar{\kappa}_a}{Pe},$$

and equating real terms leads to the following explicit expression for the growth rate σ_R in terms of the sign parameter s, Pe and Γ:

$$\sigma_R = \frac{a^2}{Pe}\left(s - a^2\Gamma\right). \tag{5.31}$$

For $s = -1$, $\sigma_R < 0$ for all such travelling-wave disturbances and for $s = +1$, $\sigma_R > 0$ for

$$0 < a^2 < \frac{1}{\Gamma} \tag{5.32}$$

i.e. the planar solution is linearly unstable with respect to perturbations with wavenumbers in the range (5.32) in the supercritical case. We note that this is consistent with the linear stability analysis where the marginal stability curve (5.21) has an asymptote at $a^2 = \frac{1}{\Gamma}$ and the planar interface is stable for all wavenumbers $a^2 > \frac{1}{\Gamma}$.

Wollkind and Segel (1970) and Caroli et al (1982) have studied the nonlinear stability of a similar set of equations in the context of alloy solidification and found that as the segregation coefficient k_s approaches zero, the instabilities are subcritical, clearly due to the enhancement of constitutional supercooling, which in our system is driven by the efficiency of premelting induced rejection of particles. Abrupt transitions to instability were observed in experiments on solidification of bentonite (Peppin et al 2008) indicating that the instability may indeed be subcritical. Owing to experimental uncertainties, however, it was not possible to determine if M was less than 1 at the transition. Future more careful experiments are needed to determine the sign of s at the onset of instability.

6. Discussion

We have studied the morphological instability of an ice–colloid interface, with vanishing segregation coefficient, including the effects of interfacial curvature, kinetic undercooling and kinetic anisotropy. Essential aspects of our work are associated with the nonlinear freezing temperature curve. We explore the regime $T > T_B$ where T_B is the critical breakthrough temperature away from the shrinkage limit $\phi \to \phi_p$ in (2.3) so that the diffusivity D can be treated as a constant. The linear stability analysis of the unidirectional solidification problem reveals the growth rate of travelling-wave instabilities in terms of the Peclet number Pe, the morphological number M, the surface energy parameter Γ, the kinetic undercooling parameter $\hat{\kappa}_u$ and the kinetic anisotropy parameter $\hat{\kappa}_a$. This allows us to explicitly demarcate the linearly stable and unstable regions in the (α, M)-plane where α is the wavenumber of the travelling-wave disturbance. The weakly nonlinear analysis leads to an evolution equation for the interface shape in terms of Pe, Γ, $\bar{\kappa}_a$ and ω, where ω is a measure of the nonlinearity of the freezing temperature curve, or colloidal liquidus.

It is useful to summarize some implications of these results for the tendency of segregated ice to form during freezing of colloidal suspensions and soils ("frost susceptibility"). In soils, the formation of segregated ice is often undesirable owing to

deleterious effects on roads and buildings (frost heave and/or thaw consolidation). On the other hand, segregated ice, or other solid, is desirable in industrial colloidal suspensions, as it enables the freeze fabrication of novel microaligned porous materials. Thus it is necessary to establish conditions under which ice segregation will occur. A main conclusion is that the onset of constitutional supercooling is an important factor determining the tendency of segregated ice to appear. Other crucial factors, such as premelting, have been elucidated before. Here we summarize what we believe to be four essential criteria for the frost susceptibility of colloidal suspensions and hence of many natural soils:

(i) The ice must premelt against the particle surface (Dash et al 2006). This allows for the segregation coefficient k_s to be zero at slow freezing velocities, hence enabling the ice to push particles rather than engulf them.

(ii) The confining pressure on the particle matrix must be such that $\phi_0 < \phi_B$. If $\phi_0 \geq \phi_B$, then no ice will form in the system until the temperature drops below T_B, at which point the ice will simply invade the pore space and the morphological instability considered here will not occur.

(iii) The freezing velocity must be less than the critical engulfment velocity V_c. Otherwise the particles are trapped by the ice due to rapid freezing (Uhlmann et al 1964; Rempel and Worster 1999; Wettlaufer and Worster 2006).

(iv) The freezing conditions must be such that constitutional supercooling occurs ahead of the ice interface.

Small temperature gradients, and high colloid-content soils (leading to large gradients in particle fraction ahead of the interface), both enhance the tendency for constitutional supercooling to occur. If all conditions are met except for the supercooling criterion (iv), one may expect to observe a stable layer of ice growing at the cooled boundary of the soil, and segregated ice will not invade the soil interior. Condition (iv) should be treated as a bound on freezing conditions, in that it is possible that the ice interface may become unstable even before constitutional supercooling has occurred (subcritical instability). In contrast to this, the volumetric expansion caused by the density difference between ice and suspension will drive a flow toward the positive z direction, expanding the colloid boundary layer and diminishing the tendency for constitutional supercooling to occur. The effects of latent heat and differing thermal conductivities between ice and particles, while not important in the system considered here, may modify the instability condition in other systems, and should be accounted for to insure system specific quantitative predictions. Many future questions present themselves, ranging from (a) solely mathematical questions regarding the quantitative and qualitative nonlinear evolution of such systems, with their possibly system specific compressibility of the colloidal matrix, (b) the complete study of the morphological instability near the shrinkage limit $\phi \to \phi_p$ in (2.3) where the diffusivity changes dramatically, (c) the extension of the model to other particularly environmentally relevant clays and silts and (d) engineering patterned composite materials be they lamellar, polygonal or otherwise orthotropic.

7. Acknowledgements

This research was supported by the King Abdullah University of Science and Technology (KAUST), Award No. KUK-C1-013-04, by the U.S. National Science Foun-

dation (0PP0440841), and by the Department of Energy (DE-FG02-05ER15741). J.S.W. is grateful for support from the Wenner-Gren Foundation, the Royal Institute of Technology and NORDITA all in Stockholm.

References

Acker, J. P., Elliott, J. A. W. & McGann, L. E. 2001 Intercellular ice propagation: Experimental evidence for ice growth through membrane pores. *Biophysical Journal* **81**, 1389–1397.

Brown, S. C. 1984 *Soil Freezing*. PhD Thesis, University of Reading, UK.

Brown, S. C. & Payne, D. 1990 Frost action in clay soils. II. Ice and water location and suction of unfrozen water in clays below 0 °C. *J. Soil Sci.* **41**, 547–561.

Caroli, B., Caroli, C. & Roulet, B. 1982 On the emergence of one-dimensional front instabilities in directional solidification and fusion of binary mixtures. *J. Physique* **43**, 1767–1780.

Chamberlain, E. J. & Gow, A. J. 1979 Effect of freezing and thawing on the permeability and structure of soils. *Eng. Geol.* **13**, 73–92.

Cisse, J. & Bolling, G. F. 1971 A study of the trapping and rejection of insoluble particles during the freezing of water. *J. Cryst. Growth* **10**, 67–76.

Dash, J.G., Rempel, A. W. and Wettlaufer, J. S. 2006 The physics of premelted ice and its geophysical consequences. *Reviews of Modern Physics* **78**, 695–741.

Davis, S. H. 2001 *Theory of Solidification*, UK: Cambridge University Press.

Defay, R. Prigogine, I. 1966 *Surface Tension and Adsorption*, London: Longmans.

Deville, S. et al. 2009 submitted.

Dong, L. & Johnson, D. T. 2004 The study of the surface tension of charge-stabilized colloidal dispersions. *Journal of dispersion science and technology* **25**, 575–583.

Hallett, J. 1963 The temperature dependence of the viscosity of supercooled water. *Proc. Phys. Soc.* **82**, 1046–1050.

Low, P. F., Anderson, D. M. & Hoekstra, P. 1968 Some thermodynamic relationships for soils at or below the freezing point. 1. Freezing point depression and heat capacity. *Water Resour. Res.* **4**, 379–394.

Nagashima, K. & Furukawa, Y. 1997 Nonequilibrium effect of anisotropic interface kinetics on the directional growth of ice crystals. *Journal of Crystal Growth* **171**, 577–585.

Novich, B. E. & Ring, R. A. 1984 Colloid stability of clays using photon correlation spectroscopy. *Clay. Clay Miner.* **32**, 400–406.

Peppin, S. S. L., Elliott, J. A. W. & Worster, M. G. 2006 Solidification of colloidal suspensions. *J. Fluid Mech.* **554**, 147–166.

Peppin, S. S. L., Worster, M. G. & Wettlaufer, J. S. 2007 Morphological Instability in freezing colloidal suspensions. *Proc. Roy. Soc. Lond. A* **463**, 723–733.

Peppin, S. S. L., Wettlaufer, J. S. & Worster, M. G. 2008 Experimental verification of morphological instability in freezing aqueous colloidal suspensions. *Phys. Rev. Lett.* **100**, 238301.

Prigogine, I. & Defay, R. 1954 *Chemical Thermodynamics*, UK: Longmans, Green and Co.

Rempel, A. W. & Worster, M. G. 1999 The Interaction between a particle and an advancing solidification front. *J. Cryst. Growth* **205**, 427–440.

Russel, W. B., Saville, D. A., & Schowalter, W. R. 1989 *Colloidal Dispersions*, UK: Cambridge University Press.

Schramm, L. L. & Helper, L. G. 1994 Surface and interfacial tensions of aqueous dispersions of charged colloidal (clay) particles. *Can. J. Chem.* **72**, 1915–1920.

Shanti, N. O., Araki, K. & Halloran, J. W. 2006 Particle redistribution during dendritic solidification of particle suspensions. *J. Am. Ceram. Soc.* **89**, 2444–2447.

Sivashinsky, G. I. 1983 On cellular instability in the solidification of a dilute binary alloy. *Physica D* **8**, 243–248.

Taber, S. 1929 Frost heaving. *J. Geol.* **34**, 428–461.

Uhlmann, D. R., Chalmers, B, & Jackson, K. A. 1964 Interaction between particles and a solid/liquid interface. *J. Appl. Phys.* **35**, 2986–2992.

Watanabe, K. & Mizoguchi, M. 2000 Ice configuration near a growing ice lens in a freezing porous medium consisting of micro glass particles. *J. Cryst. Growth* **213**, 135–140.

Watanabe, K. 2002 Relationship between growth rate and supercooling in the formation of ice lenses in a glass powder. *J. Cryst. Growth* **237-239**, 2194–2198.

White, L. R. 1982 Capillary rise in powders *J. Colloid Int. Sci.* **90**, 536–538.

Wollkind, D. J. & Segel, L. A. 1970 A nonlinear stability analysis of the freezing of a dilute binary alloy *Philosophical Transactions of the Royal Society of London A* **268**, 351–380.

Wettlaufer, J. S. 1992 Singular behavior of the neutral modes during directional solidification *Physical Review A* **46**, 6568–6578.

Wettlaufer, J. S. & Worster, M. G. 2006 Premelting dynamics *Annual Review of Fluid Mechanics* textbf38, 427–452.

Young, G. W., Davis, S. H. & Brattkus, K. 1987 Anisotropic interface kinetics and tilted cells in unidirectional solidification *J. Cryst. Growth* **83**, 560–571.

RECENT REPORTS

2009

01/09	A Mass and Solute Balance Model for Tear Volume and Osmolarity in The Normal And The Dry Eye	Gaffney Tiffany Yokoi Bron
02/09	Diffusion and permeation in binary solutions	Peppin
03/09	On the modelling of biological patterns with mechanochemical models: insights from analysis and computation	Moreo Gaffney Garcia-Aznar Doblare
04/09	Stability analysis of reaction-diffusion systems with timem-dependent coefficients on growing domains	Madzvamuse Gaffney Maini
05/09	Onsager reciprocity in premelting solids	Peppin Spannuth Wettlaufer
06/09	Inherent noise can facilitate coherence in collective swarm motion	Yates *et al.*
07/09	Solving the Coupled System Improves Computational Efficiency of the Bidomain Equations	Southern Plank Vigmond Whiteley
08/09	Model reduction using a posteriori analysis	Whiteley
09/09	Equilibrium Order Parameters of Liquid Crystals in the Laudau-De Gennes Theory	Majumdar
10/09	Landau-De Gennes theory of nematic liquid crystals: the Oseen-Frank limit and beyond	Majumdar Zarnescu
11/09	A Comparison of Numerical Methods used for Finite Element Modelling of Soft Tissue Deformation	Pathmanathan Gavaghan Whiteley
12/09	From Individual to Collective Behaviour of Unicellular Organisms: Recent Results and Open Problems	Xue Othmer Erban
13/09	Stochastic modelling of reaction-diffusion processes: algorithms for bimolecular reactions	Erban Chapman
14/09	Chaste: a test-driven approach to software development for physiological modelling	Pitt-Francis *et al.*

15/09	Block triangular preconditioners for PDE constrained optimization	Rees Stoll
16/09	From microscopic to macroscopic descriptions of cell migration on growing domains	Baker Yates Erban
17/09	The Influence of Gene Expression Time Delays on Gierer-Meinhardt Pattern Formation Systems	Seirin Lee Gaffney Monk
18/09	Analysis of a stochastic chemical system close to a sniper bifurcation of its mean field model	Erban *et al.*
19/09	On the existence and the applications of modified equations for stochastic differential equations	Zygalakis
20/09	Pebble bed: reflector treatment and pressure velocity coupling	Charpin *et al.*
21/09	A finite difference method for free boundary problems	Fornberg
22/09	Tangent unit-vector fields: nonabelian homotopy invariants and the Dirichlet energy	Majumdar Robbins Zyskin

Copies of these, and any other OCCAM reports can be obtained from:

Oxford Centre for Collaborative Applied Mathematics
Mathematical Institute
24 - 29 St Giles'
Oxford
OX1 3LB
England
www.maths.ox.ac.uk/occam